Originally published as:

Fragmented Indian plate and vertically coherent deformation beneath eastern Tibet

Savas Ceylan,[1] James Ni,[2] John Y. Chen,[3] Qie Zhang,[4,5] Frederik Tilmann,[6,7] and Eric Sandvol[1]

[1]   Using fundamental mode Rayleigh waves from the INDEPTH-IV and Namche-Barwa seismic experiments for periods between 20 and 143 s, we have investigated the lithospheric structure beneath eastern Tibet. We have found a ~200-km-wide high velocity body, starting at ~60 km depth and roughly centered beneath the Bangong-Nijuang Suture, which is most likely a piece of the underthrusting Indian continental lithosphere. The sub-horizontal underthrusting of the Indian lithosphere beneath eastern Tibet appears to be accompanied by its lateral tearing into at least two fragments, and subsequent break-off of the westernmost portion at ~91°E-33°N. The uppermost mantle low velocity zone we observe beneath the N. Qiangtang and Songpan-Ganzi terranes is most probably due to warmer and thinner lithosphere relative to southern Tibet. We attribute the low velocity zones concentrated along the northern and southern branches of the eastern Kunlun fault at lithospheric depths to strain heating caused by shearing. The azimuthal fast directions at all periods up to 143 s (~200 km peak sensitivity depth) beneath the N. Qiangtang and Songpan-Ganzi terranes are consistent, suggesting vertically coherent deformation between crust and uppermost mantle. Furthermore, the low velocity zone below the Kunlun Shan reaching down to >200 km argues against a present southward continental subduction along the southern margin of Qaidam Basin.

1. Introduction

[2]   Collision between the Indian and Eurasian plates ~50 Ma [*Argand*, 1924; *Molnar and Tapponnier*, 1975; *Yin and Harrison*, 2000] has led to the formation of the world's largest and highest continental landform: the Tibetan Plateau. Despite numerous studies over the last two decades, the dominant mechanism for the deformation and uplift of the Tibetan Plateau is still being debated. The growth and dynamics of this highly studied, yet poorly understood continental collision are commonly attributed to four different but not necessarily mutually exclusive geodynamic models: escape tectonics along major strike-slip faults and southward continental subduction [*Tapponnier et al.*, 2001], wholesale underthrusting of the Indian plate [*Argand*, 1924; *Ni and Barazangi*, 1984; *Zhou and Murphy*, 2005], ductile flow at mid- to lower crustal depths [*Clark et al.*, 2005; *Clark and Royden*, 2000], and coherent deformation between the crust and lithospheric mantle [*Bendick and Flesch*, 2007; *Silver*, 1996].

[3]   Evidence from gravity [*Jiménez-Munt et al.*, 2008], body wave tomography [*Tilmann et al.*, 2003; *Zhou and Murphy*, 2005], Pn velocity [*Liang and Song*, 2006; *McNamara et al.*, 1997], shear wave splitting [*Chen et al.*, 2010; *Huang et al.*, 2000], and receiver function [*Kind et al.*, 2002] studies strongly suggests that southern Tibet is underlain by relatively colder, more rigid Indian continental lithosphere, possibly extending past the Bangong-Nijuang Suture (BNS; see Figure 1). Images obtained by P-to-S conversions along a NS trending profile at ~85°E [*Nabelek et al.*, 2009] show indications of Indian lower crust beneath Tibet beyond the Indus-Yarlung suture (IYS) to ~31°N. Another P-to-S conversion study by *Kosarev et al.* [1999] presents evidence for northward dipping Indian lithosphere beneath southern Tibet. Similarly, P wave tomography results from INDEPTH-III (InterNational DEep Profiling of Tibet and the Himalayas) seismic experiment

[1]Department of Geological Sciences, University of Missouri, Columbia, Missouri, USA.
[2]Department of Physics, New Mexico State University, Las Cruces, New Mexico, USA.
[3]Institute for Theoretical and Applied Geophysics, Peking University, Beijing, China.
[4]Subsurface Technology, BP America, Houston, Texas, USA.
[5]Formerly at Department of Geological Sciences, University of Missouri, Columbia, Missouri, USA.
[6]Helmholtz-Centre Potsdam, GFZ German Research Centre for Geosciences, Potsdam, Germany.
[7]Institute of Geological Sciences, Freie Universität Berlin, Berlin, Germany.

Corresponding author: S. Ceylan, Department of Geological Sciences, University of Missouri, 101 Geology Bldg., Columbia, MO 65211, USA. (savas.ceylan@mail.missouri.edu)
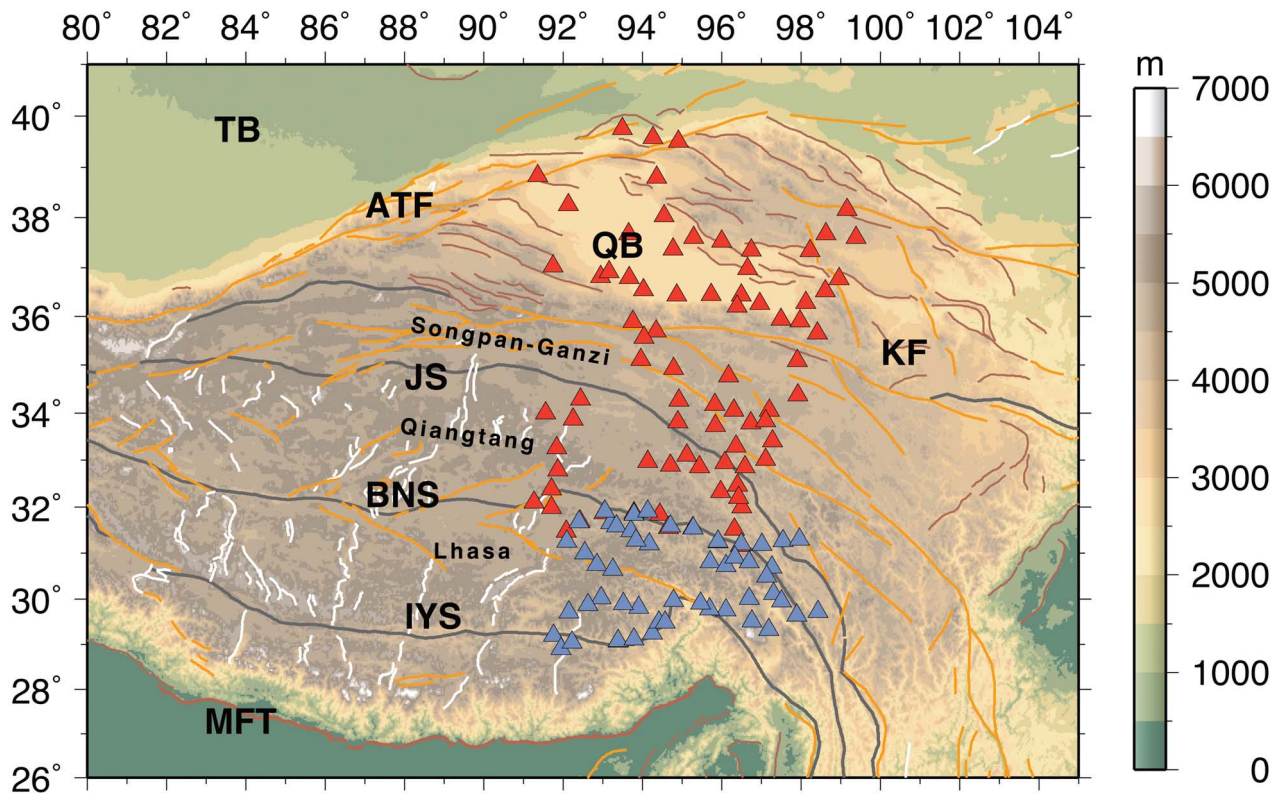
Figure 1. Seismic station locations (red triangles are INDEPTH-IV stations, blue triangles indicate Namche-Barwa stations) with tectonic features [*Styron et al.*, 2010]. White and brown lines show normal and thrust faults, respectively. Orange lines represent strike-slip faults. Suture zones are marked by thick gray lines. IYS: Indus-Yarlung suture; BNS: Bangong-Nujiang Suture; JS: Jinsha Suture; KF: Kunlun Fault; QB: Qaidam Basin; TB: Tarim Basin; ATF: Altyn-Tagh Fault; and MFT: Main Frontal Thrust.

[*Tilmann et al.*, 2003] reveal a sub-vertically downwelling high velocity body beneath BNS interpreted as a part of the underthrusting Indian continental lithosphere (UICL). S-to-P conversion [*Kumar et al.*, 2006; *Zhao et al.*, 2010] and body wave tomography [*Li et al.*, 2008; *Liang et al.*, 2012] studies demonstrate that the E-W geometry and thickness of the underthrusting Indian plate is significantly variable. Further north, slow Pn and inefficient Sn waves north of the BNS are interpreted as warmer uppermost mantle [*Barazangi and Ni*, 1982; *Ni and Barazangi*, 1984]. In contrast to these observations and in support of the wholesale underthrusting/ subduction model, global body wave tomography images [*Zhou and Murphy*, 2005] and some continent-scale surface wave models [*Priestley et al.*, 2006] show fast upper mantle velocities beneath most of Tibet, suggesting that the UICL has subducted sub-horizontally beneath the entire plateau to depths of ~200 km, and has a variable lateral geometry and dip. Additionally, P [*Kind et al.*, 2002] and S [*Zhao et al.*, 2011] receiver function images show an apparent southward continental subduction south of the Qaidam Basin.

[4] Due to insufficient coverage of existing seismic experiments in the Plateau, the nature and northward extent of the subducted Indian plate, and structure beneath the Plateau are not well known. Additionally, a comparison of

previous surface and body wave tomography results [*Li et al.*, 2008] shows significant discrepancies beneath southeastern Tibet. Here, in order to further constrain the dominant deformational mechanisms within the Plateau and the geometry of the UICL, we present a new Rayleigh wave tomography model based on the INDEPTH-IV and Namche-Barwa [*Sol et al.*, 2007] experiments (Figure 1) in north-central and southeastern Tibet, respectively. We address the following: (1) what is the northward extent of the UICL and what is its geometry, (2) is there southward continental subduction south of the Qaidam Basin, and (3) what is the horizontal finite strain fabric beneath eastern Tibet and is there evidence for vertically coherent deformation?

2. Data and Methods

[5] We use fundamental mode Rayleigh waves and two-plane wave tomography (TPWT) for phase velocity inversions [*Forsyth and Li*, 2005]. We choose earthquakes with epicentral distances between 20° and 120°, depth ≤100 km, and $M_S \geq 5.7$. We only use the vertical component in order to avoid shear and Love wave interference, and long period noise that may exist on horizontal components. The events with low signal to noise (S/N) ratios are eliminated visually. Our data was recorded from INDEPTH-IV array (74 broadband
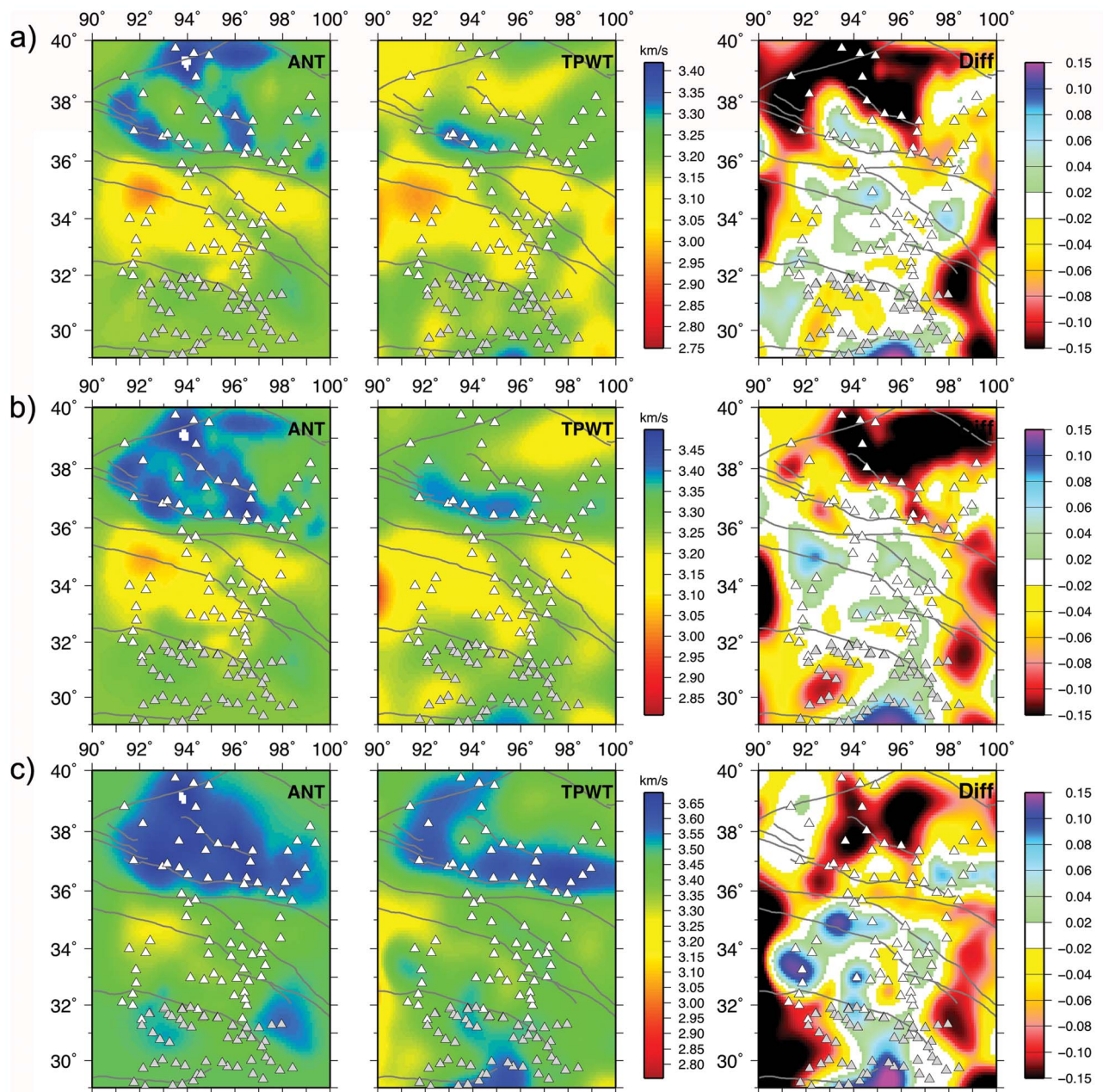
Figure 2. The difference between isotropic phase velocities obtained using ambient noise tomography (ANT) [*Yang et al.*, 2010] and two-plane wave approach (TWPT) for periods of (a) 25, (b) 30, and (c) 40 s. The third column shows the difference between two methods in km/s. These results show that within the seismic array (with the exception of Qaidam Basin), phase velocities obtained by two methods are similar (∼±0.06 km/s).

stations) that was deployed across Northern Tibet (Figure 1). We have also included data from the Namche-Barwa seismic array [*Sol et al.*, 2007] in southeastern Tibet. Prior to data processing, all instrument responses are converted to the first generation STS2. We measure phase velocities for 13 frequency bands ranging between 20 and 143 s, and utilize 10-mHz-wide Butterworth filters centered on each frequency. In order to avoid dependence on earthquake magnitude, we

normalize the seismic wave amplitude for each event, then measure phases and amplitudes of visually windowed data using Fourier analysis. We have used a total of 174 earthquakes. In order to increase the reliability of our inversions, we only include events that were recorded by at least 10 stations.

[6] The first step in our inversions is calculating isotropic phase velocities for each frequency. Our experiments with TPWT show that ∼60 events are enough to obtain stable
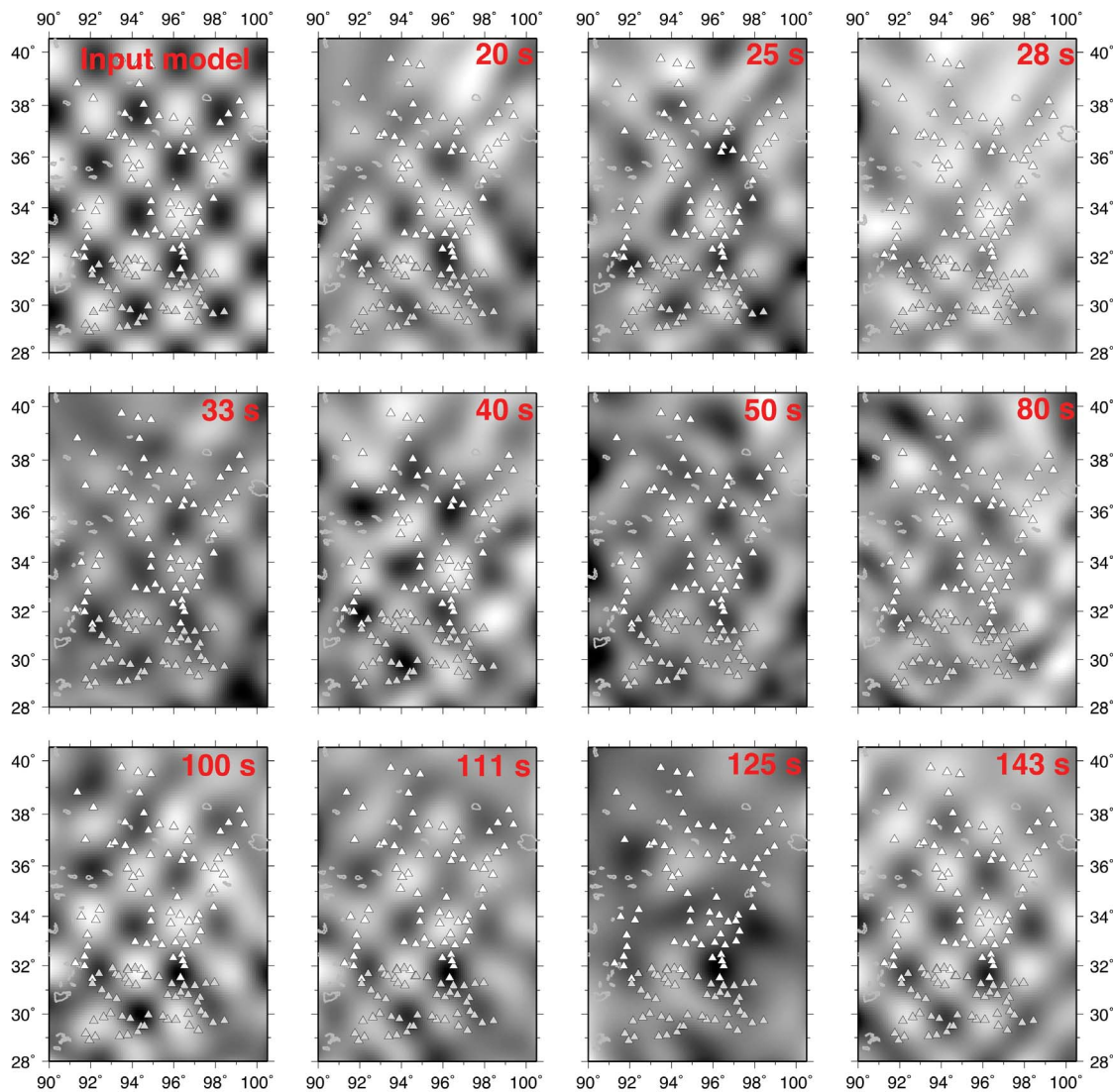
Figure 3. The resolution test results for different periods using checkerboard synthetic model. The anomalies in the input model are $1.5° \times 1.5°$. The periods are indicated in upper-right corner of each panel.

results. However, in order to better constrain our inversion parameters (i.e., smoothing length and damping), we compare our results with those of Ambient Noise Tomography (ANT) [*Yang et al.*, 2010]. Although both methods measure surface wave dispersion, ANT and TPWT are fundamentally different and use independent data sets: TPWT implements surface waves created by earthquakes while ANT excludes earthquakes and uses ambient noise of the earth. Additionally, while ANT uses ray theory to obtain phase maps, TPWT assumes that distortion of wavefronts at each station can be expressed as the sum of two plane waves [*Forsyth and Li*, 2005]. Due to the short wavelengths of ambient surface waves, ANT can typically obtain more reliable results at crustal depths than TPWT. There is an overlapping frequency range between these two methods (in our case 20–50 s). The comparison of isotropic phase velocities indicates that within the seismic array, these two methods reveal very similar results (differences less than ±0.06 km/s with the exception

of Qaidam Basin) for periods between 25 and 40 s (Figure 2). With the exception of 125 s (~170 km), the checkerboard tests (Figure 3) imply that resolution within the seismic array is ~150 km or better at all periods, sufficient to image all of the anomalies discussed in this study. However, due to insufficient raypaths from the W-NW (auxiliary material Figure S1), the checkerboard tests exhibit evidence for some lateral smearing.[1]

[7] The second step of phase velocity inversion includes determining anisotropic phase velocities and seismic fast directions (Figure 4). Unlike traditional ray theory, TPWT accounts for phase and amplitude changes. A disadvantage of this method is its sensitivity to finite frequency effects such as scattering and wavefront healing [*Hung et al.*, 2001;

---

[1]Auxiliary materials are available in the HTML. doi:10.1029/2012JB009210.
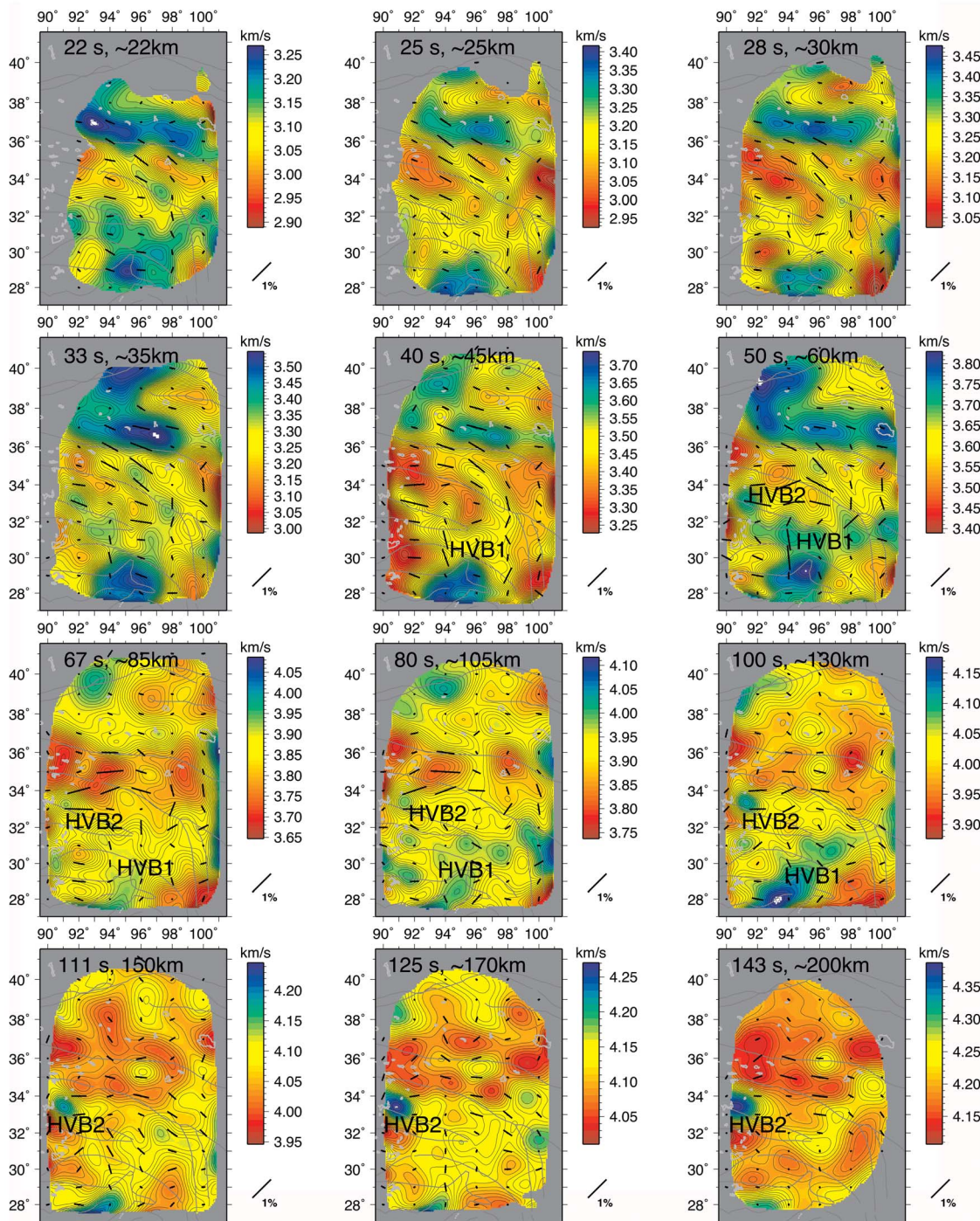
Figure 4. Anisotropic phase velocity maps for 12 periods (22–143 s). The solid black lines indicate azimuthal fast direction and amplitude of anisotropy. Note that color scales are different for each map. The regions with errors of $2\sigma \leq 0.06$ km/s (where σ is the standard deviation) are shaded. HVB1 and HVB2 show the high velocity bodies addressed in the text.

Nolet and Dahlen, 2000]. To overcome these limitations, we employ 2D sensitivity kernels [*Yang and Forsyth*, 2006] for both amplitude and phase perturbation for each period. Azimuthal anisotropy is simultaneously solved with Rayleigh wave phase velocities. Since the shortest wavelength for our data is ~65 km (for 20 s period and taking average phase velocity as 3.18 km/s), we use a constant smoothing length of 80 km for all periods. There is always a trade-off between lateral heterogeneity of isotropic phase maps and anisotropy. In order to reduce the effects of this trade-off, we use high
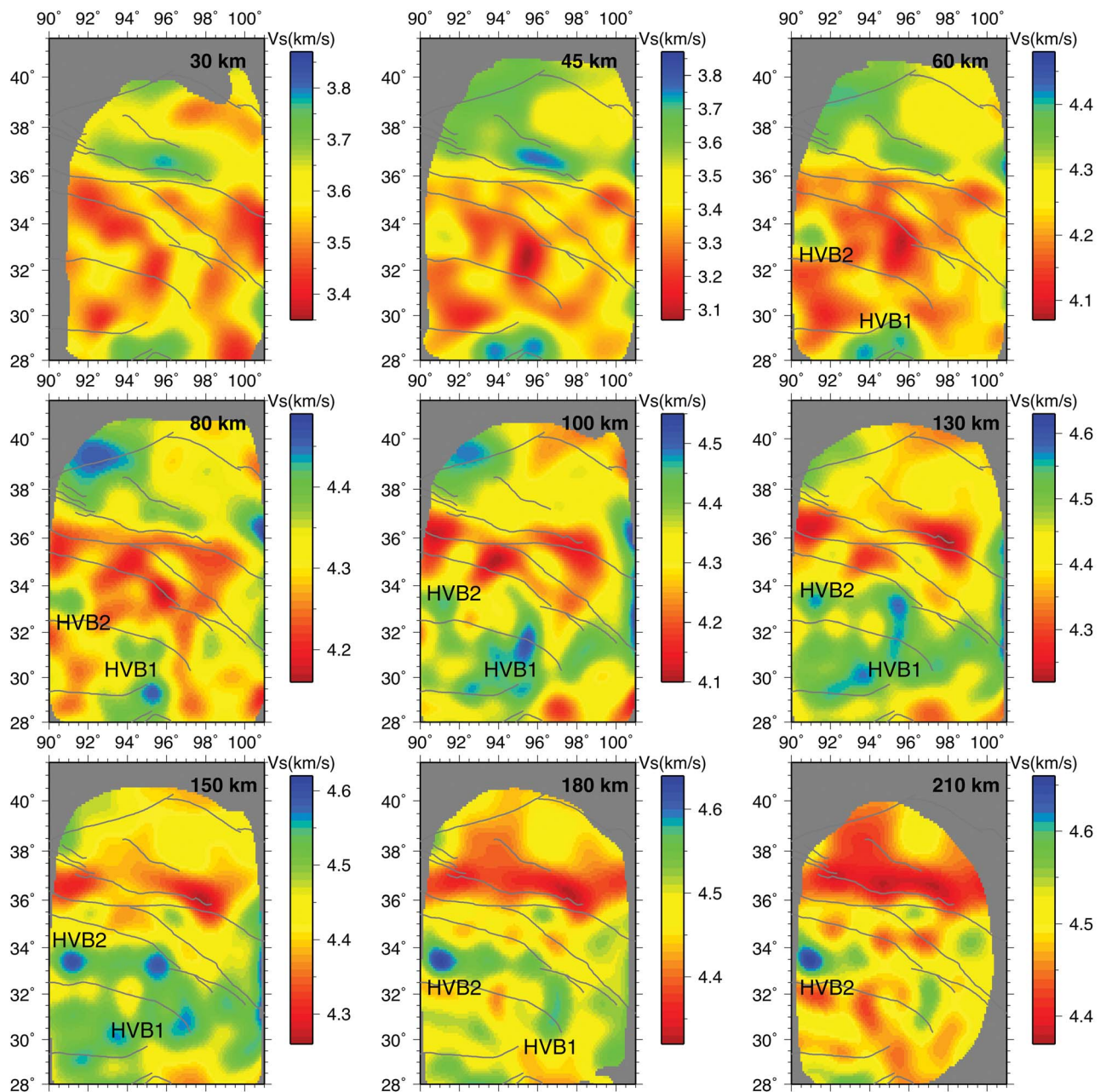
Figure 5. Shear wave velocities (km/s) for depths between 30 and 210 km. Depths are indicated on each panel. Note that each panel has a different color scale. The dark gray lines show major tectonic features. HVB1 and HVB2 are the same as referenced to in the text. The regions with errors of $2\sigma \leq 0.06$ km/s (where σ is the standard deviation) are shaded, based on peak depth sensitivity of corresponding frequencies. An unmasked version of this image is provided in auxiliary material Figure S6.

damping both for anisotropy and phase velocities. We have tested our inversion results by using a variety of damping values. However, the final choice of damping parameter was made considering model uncertainties (auxiliary material Figure S2) and consistency with ANT results. Moreover, the features we discuss here are consistently observed in all inversions regardless of damping. Additionally, to increase reliability, we only interpret phase velocities with errors $2\sigma \leq 0.06$ km/s, where σ is the standard deviation.

[8] The third and last step of the inversion is obtaining shear wave velocities (Figures 5 and 6) using the anisotropic phase maps from the second step. For shear wave inversions, we use the partial derivatives from *Saito* [1988]. For the initial model, the AK135 model is adapted to our region by taking average Moho depths of 45 and 60 km for Qaidam Basin and the rest of the region [*Zhu and Helmberger*, 1998], respectively. We defined 50 layers for shear wave inversion from the surface to 400 km depth. According to *Li*
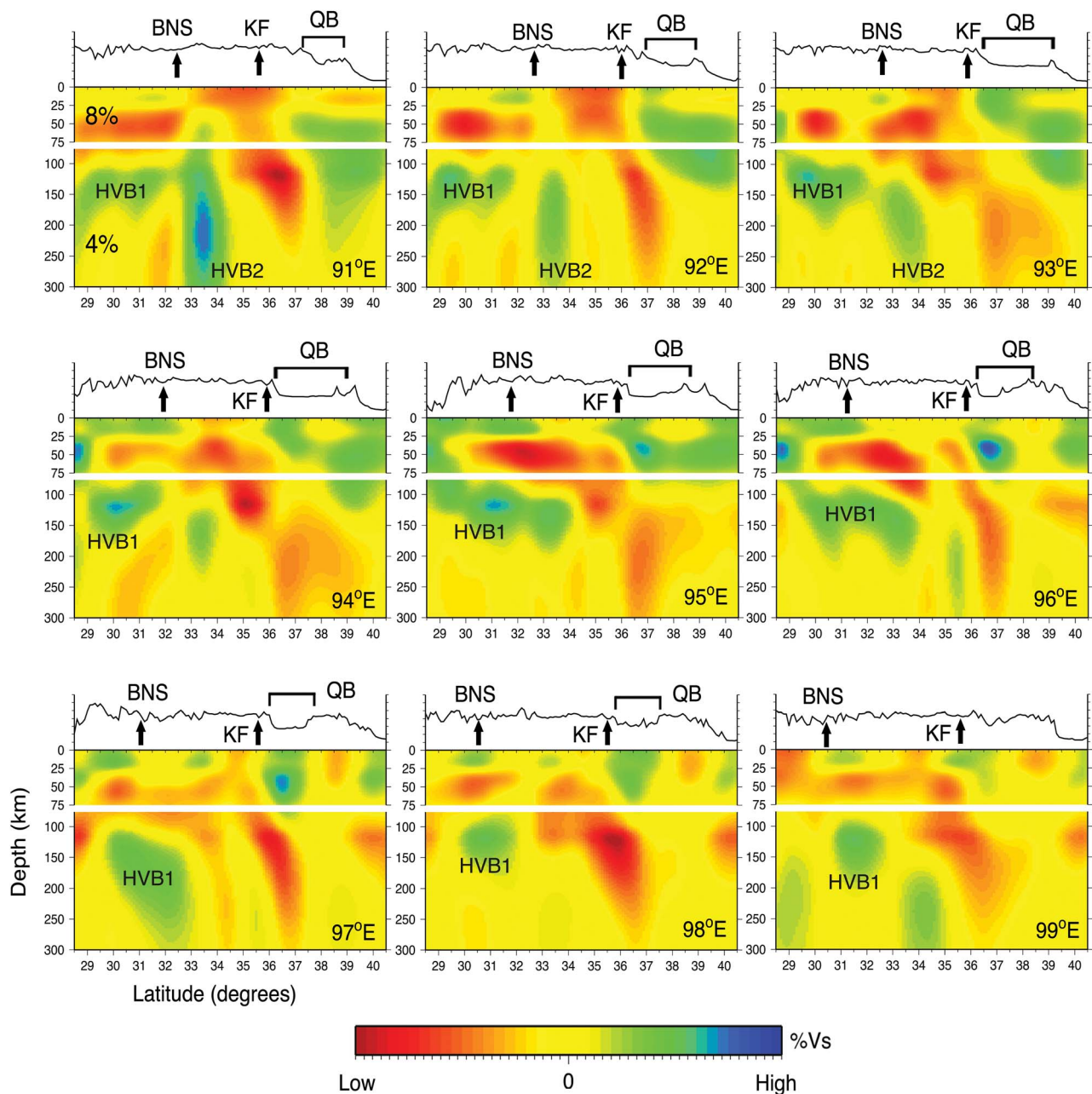
Figure 6. Shear wave (SV) anomalies along 91°E–99°E. 0–75 km and 75–300 km depth ranges were colored using 8% and 4% variation according to the mean value at each depth, respectively. Major structures are marked on the topography profiles for each profile. For additional profiles see supplementary materials. HVB1 and HVB2 indicate the high velocity bodies discussed in the text. Other abbreviations are the same as Figure 1.

[2011], who used a similar frequency range with less data, the shear wave structure cannot be determined precisely at all layers, but the average velocity for each defined layer can be resolved for depths less than 250 km. Therefore, we do not interpret our results for depths >200 km.

3. Results

[9] Figures 4–6 show our tomographic models for Rayleigh wave phase and shear wave velocities. Starting from the south, we observe a high velocity body (HVB1) along the BNS and further south, between the depths of ∼60 and 170 km. This feature is highly heterogeneous in the east-west direction with a shear wave anomaly of ≥2%. Furthermore, the phase velocity maps (Figure 4) show regions of relatively low velocities within the HVB1. The shear wave anomaly cross-sections (Figure 6) demonstrate that the HVB1 has a sub-horizontal geometry dipping northward slightly beneath the BNS, between ∼94°E and 97°E. A further isolated high velocity body (HVB2) is observed at ∼91°E-33°N which
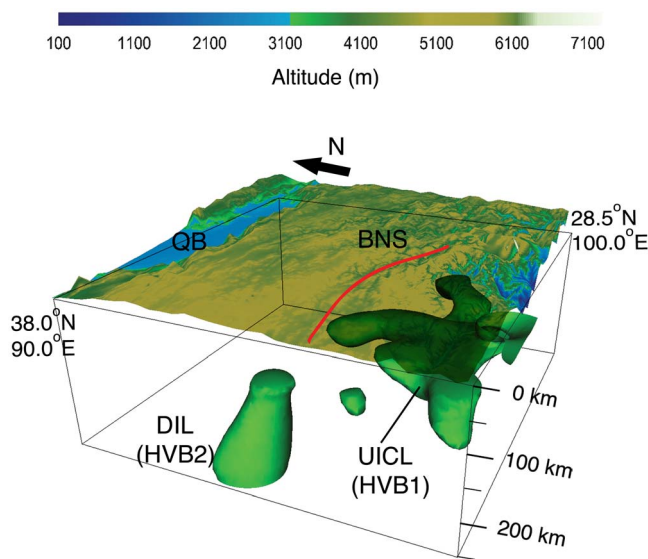
Figure 7. Isosurface for 2% faster shear waves for 60 km and deeper, overlain by topography (28.5°–38.0°N and 90.0°–100.0°E). Altitudes are shown by color scale (at top). QB: Qaidam Basin; BNS (red line): Bangong-Nujiang Suture; DIL: Detached Indian Lithosphere (referred to as HVB2 in the text); UICL: Underthrusting Indian continental lithosphere (referred to as HVB1 in the text). View from azimuth 245° and tilt 67° from vertical. A video of this image is provided in the auxiliary material (Animation S1).

appears to be connected to the HVB1 beneath the BNS at ~130–150 km, becoming isolated again at greater depths. This vertically continuous feature starts at ~60 km depth (50 s) and gradually increases in diameter to depths greater than 200 km (Figures 4 and 5).

[10] Further north, low velocities characterize the uppermost mantle beneath the N. Qiangtang and Songpan-Ganzi. The shear wave velocities are ~4% slower than those observed beneath the Lhasa block and southern Qiangtang terrane (Figure 5). Anisotropic fast directions (Figure 4) across the northern and southern branches of the Kunlun Fault tend to conform to strikes of the active faults (±15°). We also observe the largest amplitude of azimuthal anisotropy across these shear zones. Seismic anisotropy appears to be consistent at depth (±15°) with the exception of the southeast portion of our region. Similar to shear wave splitting measurements [*Huang et al.*, 2000; *León Soto et al.*, 2012], azimuthal fast directions exhibit a general clockwise rotation (auxiliary material Figures S3 and S5).

[11] Both phase maps and S wave anomalies (Figure 6) show ~1% higher velocities, indicating thicker (~130–140 km) and possibly rigid lithosphere beneath the Qaidam Basin. We also observe the eastern edge of the Tarim Basin (auxiliary material Figure S4). In an approximate agreement with the lithosphere-asthenosphere boundary (LAB) phases of S-wave receiver functions [*Zhao et al.*, 2011], the Tarim Basin has a lithospheric thickness of ~200 km, while the Qaidam Basin is substantially thinner. Beneath the Kunlun Shan, south of Qaidam Basin, we observe low velocity zones that are concentrated along the northern and southern branches of the Kunlun Fault, extending deeper than 200 km.

[12] Comparisons with independent phase maps using ambient noise [*Yang et al.*, 2010] suggest that we are able to measure the phase velocities with a high degree of precision (differences less than 0.06 km/s within the array, Figure 2). Furthermore, unlike previous surface and body wave measurements [*Li et al.*, 2008], our shear wave observations are broadly consistent with those obtained using body wave tomography [*Liang et al.*, 2012]. Moreover, the comparison of the splitting data from *León Soto et al.* [2012] and our azimuthal fast directions for 143 s shows that average differences are ~14° and 10° for Qiangtang and Songpan-Ganzi, respectively (auxiliary material Figure S5).

4. Discussion

4.1. High Velocity Body Beneath Lhasa and Southern Qiangtang Terrane

[13] Presuming that the Indian plate does not extend substantially past the BNS, the high velocity body (HVB1) in our images beneath the BNS could be explained by large-scale delamination of the Eurasian plate. However, considering the compelling evidence for the continuation of Indian plate into the central part of the Plateau [*Kind et al.*, 2002; *Nelson et al.*, 1996; *Tilmann et al.*, 2003] as well as the lack of recent volcanism, a delamination model is not well supported. Our results reveal a low velocity zone north of the BNS at depths of ~90–200 km, indicating a thinner and possibly warmer lithosphere beneath the northern Qiangtang and Songpan-Ganzi terranes [*Haines et al.*, 2003; *Tilmann et al.*, 2003; *Zhou and Murphy*, 2005]. Along the BNS and further south, both shear wave velocity (Figures 5 and 6) and Rayleigh wave phase maps (Figure 4) indicate the presence of a high velocity body. The compatibility between these observations and those of prior studies strongly suggests that the high velocity zone underlying the BNS represents the Indian continental lithosphere. The heterogeneity of this anomaly argues against a wholesale underthrusting model [*Barazangi and Ni*, 1982] in eastern Tibet. According to the phase and shear wave velocity maps (Figures 4 and 5), the underthrusting Indian continental lithosphere (UICL) extends from lower crustal depths to ~170 km, and is very heterogeneous in the east-west direction. Because of the slight northward dip of the HVB1, the transition from fast to slow anomalies occurs almost exactly at the BNS and directly below the Moho (~80 km; Figure 5), in accordance with previous Pn velocity [*McNamara et al.*, 1997] and Sn blockage observations [*Barazangi and Ni*, 1982; *Barron and Priestley*, 2009].

[14] Based on our tomographic models (Figures 4–6), underthrusting is accompanied by lateral fragmentation of the UICL into two wings. The fragmentation initiates at ~30°N-96°E at ~100 km depth. Figure 7 shows the proposed geometry of the UICL, using a 2% faster shear wave anomaly isosurface. We suggest that the oblique collision between India and Eurasia, and oroclinal bending in the EHS may have caused the fragmentation. Flattening of the UICL during sub-horizontal underthrusting may also have influenced this fragmentation by increasing extensional stresses. Alternatively, this geometry may be a result of chemical heterogeneity within the UICL. However, our observations of average phase velocities are more consistent with a highly deformed continental lithosphere rather than a stable shield

[e.g., *Chevrot and Zhao*, 2007]. Furthermore, low phase velocities within the UICL are nearly as low as the low velocities in the north, where there clearly is no UICL.

[15] The second high velocity body (HVB2) we observe is located ∼100 km north of the BNS beneath the Qiangtang Terrane (between ∼91°–92°E) and is the strongest anomaly reaching to depths >200 km (Figure 5). This structure may result from an ongoing Rayleigh-Taylor instability of the Asian lithosphere. Given that this is the case, both its vertical position as well as its thermal state can be predicted. The most recent mafic potassic volcanism (∼13 Ma [*Turner et al.*, 1996]) in the vicinity of the HVB2 provides insight into initiation of a possible instability. In order to estimate the vertical position of the HVB2 in the mantle, we use the mechanical modeling code provided by *Gerya* [2010]. To approximate the thermal state of a cold body residing in the asthenosphere for the given amount of time, we use the heat conduction equation $\partial T/\partial t + u. \nabla T = \kappa \nabla^2 T$, where κ is temperature independent thermal diffusivity (10^{-6} m^2/s). The term $u. \nabla T$ represents the advection term, where u is convergence (or sinking) rate in m/s. We use an ambient asthenosphere temperature of 1300°C and an initial uniform temperature of 600°C for the HVB2. For our purposes, we ignore shear and radiogenic heating terms.

[16] Assuming a low mantle viscosity (10^{18} Pas), the HVB2 would be predicted to sink below depths observable by our method (>250 km). However, supposing a higher mantle viscosity (10^{21} Pas), the HVB2 would sink at a rate of ∼6.0 mm/yr [*Gerya*, 2010]. At this rate, similar to our observations, the HVB2 would have sunk ∼80 km into the asthenosphere. Using a slow rate of sinking (high viscosity), thermal conductivity modeling predicts that a delaminated HVB2 would be ∼200°C warmer (800°C) at its center, and consequently have a lower shear wave velocity. However, similar to the Indian lithosphere, the HVB2 has ∼4% higher velocity than the Songpan-Ganzi, implying that it is colder, more rigid, and may have a different composition. In light of structures with similar S-wave velocities, the observed continuous vertical geometry of the HVB2 (Figures 4–6), evidence from previous body wave and receiver function studies [*Kind et al.*, 2002; *Kosarev et al.*, 1999; *Tilmann et al.*, 2003], we interpret this body to be the northernmost extent of the UICL, possibly tearing off from the westernmost fragment. Observed both in our results and *Liang et al.* [2012], the HVB2 may be a continuation of the body observed by *Tilmann et al.* [2003] at ∼89°E, adjacent to our region to the west.

4.2. Northern Qiangtang and Songpan-Ganzi Terranes

[17] Consistent with slow Pn and inefficient Sn propagation observations [*Barazangi and Ni*, 1982; *McNamara et al.*, 1997], the N. Qiangtang and Songpan-Ganzi terranes are underlain by a low-velocity upper mantle. This low velocity anomaly correlates with Late Tertiary basaltic volcanism and has 4–4.2% slower shear wave velocities (4.3–4.4 km/s at 130 km) than those observed beneath the Lhasa block and southern Qiangtang terrane. The Qiangtang and Songpan-Ganzi have the highest amplitude seismic anisotropy with EW and NW-SE fast directions. Velocity perturbations correspond to a 300°C anomaly [*Wittlinger et al.*, 1996] in the uppermost mantle, which may be due to viscous heating [*Kincaid and Silver*, 1996] or a mantle up-welling associated with small scale convection induced by the underthrusting/

subduction of Indian lithosphere [*Tilmann et al.*, 2003]. Alternatively, very localized upwelling caused by strong coupling between the top of the asthenosphere and escaping lithosphere may have resulted in a low velocity mantle lid. However, the observed pattern of low velocities does not fit this model as well as the viscous strain heating model. The pattern of low shear wave velocities correlates well with the active faulting and regions of highest strain rate [*Gan et al.*, 2007]. The absence of a high velocity body below the northernmost plateau argues against models proposing pure shear shortening of Asian lithosphere and/or underthrusting of the UICL beneath the entire plateau.

[18] The general clockwise rotation of seismic fast directions is consistent with shear wave splitting results [*Huang et al.*, 2000; *León Soto et al.*, 2012]. Fast directions obtained from seismic anisotropy can be used as proxies for the direction of mantle finite strain, resulting from Lattice Preferred Orientation (LPO) of olivine in the upper mantle [*Montagner and Guillot*, 2002]. With the exception of the southeast portion of our region where we lose resolution, the azimuthal fast directions are consistent (±15°) at all periods, suggesting that the crust and mantle deformation is vertically coherent beneath the N. Qiangtang and Songpan-Ganzi. Furthermore, our observations evince that this coherence extends into the asthenosphere.

4.3. Kunlun Fault and Qaidam Basin

[19] Our tomographic models show low velocity zones at mid-lower crustal depths, concentrated along the two branches of the Kunlun Fault. Anisotropic fast directions (Figure 4) across these shear zones tend to conform to faults' strikes (±15°). This is more apparent at mid-upper crustal depths, indicating that shearing is the dominant deformation mechanism along these zones. Recent strain heating experiments [*Nabelek et al.*, 2010; *Whittington et al.*, 2009] demonstrate that thermal diffusivity decreases much faster with depth than previously thought. An implication of this finding includes that partial melting could be induced by trapped viscous strain heating (produced by non-brittle deformation of mantle material) along major shear zones associated with Tibetan strike-slip faults. This model is consistent with high strain rates [*Gan et al.*, 2007] and the observed low velocity zones that are centered along northern and southern branches of the Kunlun in northern Tibetan Plateau. Moreover, assuming a constant shear stress, as viscosity decreases, strain rate and viscous heating should increase. Alternatively, keeping the strain rate constant and assuming a change in viscosity decreases over time ($\partial \eta/\partial t \to 0$, where η is viscosity), strain heating becomes constant and causes a temperature anomaly [*Burg and Gerya*, 2005]. In either case, in accordance with our observations (Figure 6), it may be plausible that strain heating can extend into the asthenosphere along major shear zones beneath N. Tibet.

[20] In support of the continental subduction model, receiver functions findings [*Kind et al.*, 2002; *Kosarev et al.*, 1999] suggest a south dipping mantle converter beneath the northern margin of the Plateau. However, there is no indication of southward continental subduction or overriding of Tibetan lithosphere [*Zhao et al.*, 2011] in our tomographic models. Instead, we observe a continuous low velocity anomaly up to the Kunlun fault, south of the Qaidam Basin. These boundaries seen in receiver function images, which were interpreted to be indicative of southward continental

subduction, might instead represent preserved mantle reflectors [*Yue et al.*, 2012].

5. Conclusions

[21] Our primary conclusions are as follows:

[22] 1. We observe a high velocity structure beneath the Lhasa and southern Qiangtang down to ~170 km depth, and we interpret this anomaly as the UICL.

[23] 2. The UICL has a sub-horizontal geometry, and tears laterally into at least two fragments beneath southeastern Tibet. The westernmost branch appears to be detached and vertically sinking into the asthenosphere.

[24] 3. The uppermost mantle beneath the N. Qiangtang and Songpan-Ganzi terranes are characterized by low velocities, probably due to warmer lithosphere caused by viscous strain heating or upwelling of the astenosphere. The observed low velocity zones are concentrated along the Kunlun Fault. We attribute this observation to trapped strain heating caused by shearing. Additionally, fast directions across this shear zone tend to conform to active faults' strikes (within the range of $\pm15°$), implying that horizontal shearing is the dominant deformational mechanism.

[25] 4. Azimuthal fast directions beneath the Qiangtang and Songpan-Ganzi terranes are consistent at depth, supporting vertically coherent deformation extending from the crust into the mantle.

[26] 5. Our tomographic images outline the Qaidam Basin with ~1% higher anomalies down to depths of ~130 km. The low velocities below the Kunlun range provide evidence against continental subduction along northeastern edge of the Tibetan Plateau.

References

Argand, E. (1924), La tectonique de l'Asie, paper presented at 13th International Geological Congress, IUGS, Brussels.

Barazangi, M., and J. Ni (1982), Velocities and propagation characteristic of Pn and Sn beneath the Himalayan arc and Tibetan plateau: Possible evidence for underthrusting of Indian continental lithosphere beneath Tibet, *Geology*, *10*, 179–185, doi:10.1130/0091-7613(1982)10<179: VAPCOP>2.0.CO;2.

Barron, J., and K. Priestley (2009), Observations of frequency-dependent Sn propagation in Northern Tibet, *Geophys. J. Int.*, *179*(1), 475–488, doi:10.1111/j.1365-246X.2009.04318.x.

Bendick, R., and L. Flesch (2007), Reconciling lithospheric deformation and lower crustal flow beneath central Tibet, *Geology*, *35*(10), 895–898, doi:10.1130/G23714A.1.

Burg, J. P., and T. V. Gerya (2005), The role of viscous heating in Barrovian metamorphism of collisional orogens: Thermomechanical models and application to the Lepontine Dome in the central Alps, *J. Metamorph. Geol.*, *23*(2), 75–95, doi:10.1111/j.1525-1314.2005.00563.x.

Chen, W.-P., M. Martin, T.-L. Tseng, R. L. Nowack, S.-H. Hung, and B.-S. Huang (2010), Shear-wave birefringence and current configuration of converging lithosphere under Tibet, *Earth Planet. Sci. Lett.*, *295*(1–2), 297–304, doi:10.1016/j.epsl.2010.04.017.

Chevrot, S., and L. Zhao (2007), Multiscale finite-frequency Rayleigh wave tomography of the Kaapvaal craton, *Geophys. J. Int.*, *169*(1), 201–215, doi:10.1111/j.1365-246X.2006.03289.x.

Clark, M. K., and L. H. Royden (2000), Topographic ooze: Building the eastern margin of Tibet by lower crustal flow, *Geology*, *28*(8), 703–706, doi:10.1130/0091-7613(2000)28<703:TOBTEM>2.0.CO;2.

Clark, M. K., J. W. M. Bush, and L. H. Royden (2005), Dynamic topography produced by lower crustal flow against rheological strength heterogeneities bordering the Tibetan Plateau, *Geophys. J. Int.*, *162*(2), 575–590, doi:10.1111/j.1365-246X.2005.02580.x.

Forsyth, D. W., and A. Li (2005), Array analysis of two-dimensional variations in surface wave phase velocity and azimuthal anisotropy in the presence of multipathing interference, in *Seismic Earth: Array Analysis of Broadband Seismograms*, *Geophys. Monogr. Ser.*, vol. 157, edited by A. Levander and G. Nolet, pp. 81–97, AGU, Washington, D. C., doi:10.1029/157GM06.

Gan, W., P. Zhang, Z.-K. Shen, Z. Niu, M. Wang, Y. Wan, D. Zhou, and J. Cheng (2007), Present-day crustal motion within the Tibetan Plateau inferred from GPS measurements, *J. Geophys. Res.*, *112*, B08416, doi:10.1029/2005JB004120.

Gerya, T. (2010), *Introduction to Numerical Geodynamic Modelling*, 345 pp., Cambridge Univ. Press, Cambridge, U. K.

Haines, S. S., S. L. Klemperer, L. Brown, J. Guo, J. Mechie, R. Meissner, A. Ross, and W. Zhao (2003), INDEPTH III seismic data: From surface observations to deep crustal processes in Tibet, *Tectonics*, *22*(1), 1001, doi:10.1029/2001TC001305.

Huang, W.-C., et al. (2000), Seismic polarization anisotropy beneath the central Tibetan Plateau, *J. Geophys. Res.*, *105*(B12), 27,979–27,989.

Hung, S.-H., F. A. Dahlen, and G. Nolet (2001), Wavefront healing: A banana-doughnut perspective, *Geophys. J. Int.*, *146*, 289–312, doi:10.1046/j.1365-246x.2001.01466.x.

Jiménez-Munt, I., M. Fernandez, J. Verges, and J. Platt (2008), Lithosphere structure underneath the Tibetan Plateau inferred from elevation, gravity and geoid anomalies, *Earth Planet. Sci. Lett.*, *267*(1–2), 276–289, doi:10.1016/j.epsl.2007.11.045.

Kincaid, C., and P. Silver (1996), The role of viscous dissipation in the orogenic process, *Earth Planet. Sci. Lett.*, *142*, 271–288, doi:10.1016/0012-821X(96)00116-1.

Kind, R., et al. (2002), Seismic images of crust and upper mantle beneath Tibet: Evidence for Eurasian plate subduction, *Science*, *298*(5596), 1219–1221, doi:10.1126/science.1078115.

Kosarev, G., R. Kind, S. V. Sobolev, X. Yuan, W. Hanka, and S. Oreshin (1999), Seismic evidence for a detached Indian lithospheric mantle beneath Tibet, *Science*, *283*(5406), 1306–1309, doi:10.1126/science.283.5406.1306.

Kumar, P., X. Yuan, R. Kind, and J. Ni (2006), Imaging the colliding Indian and Asian lithospheric plates beneath Tibet, *J. Geophys. Res.*, *111*, B06308, doi:10.1029/2005JB003930.

León Soto, G., E. Sandvol, J. F. Ni, L. Flesch, T. M. Hearn, F. Tilmann, J. Chen, and L. D. Brown (2012), Significant and vertically coherent seismic anisotropy beneath eastern Tibet, *J. Geophys. Res.*, *117*, B05308, doi:10.1029/2011JB008919.

Li, A. (2011), Shear wave model of southern Africa from regional Rayleigh wave tomography with 2-D sensitivity kernels, *Geophys. J. Int.*, *185*(2), 832–844, doi:10.1111/j.1365-246X.2011.04971.x.

Li, C., R. van der Hilst, A. Meltzer, and E. Engdahl (2008), Subduction of the Indian lithosphere beneath the Tibetan Plateau and Burma, *Earth Planet. Sci. Lett.*, *274*(1–2), 157–168, doi:10.1016/j.epsl.2008.07.016.

Liang, C., and X. Song (2006), A low velocity belt beneath northern and eastern Tibetan Plateau from Pn tomography, *Geophys. Res. Lett.*, *33*, L22306, doi:10.1029/2006GL027926.

Liang, X., E. Sandvol, Y. J. Chen, T. Hearn, J. Ni, S. Klemperer, Y. Shen, and F. Tilmann (2012), A complex Tibetan upper mantle: A fragmented Indian slab and no south-verging subduction of Eurasian lithosphere, *Earth Planet. Sci. Lett.*, *333–334*, 101–111, doi:10.1016/j.epsl.2012.03.036.

McNamara, D. E., W. R. Walter, T. J. Owens, and C. J. Ammon (1997), Upper mantle velocity structure beneath the Tibetan Plateau from Pn travel time tomography, *J. Geophys. Res.*, *102*(B1), 493–505, doi:10.1029/96JB02112.

Molnar, P., and P. Tapponnier (1975), Cenozoic tectonics of Asia: Effects of a continental collision, *Science*, *189*(4201), 419–426, doi:10.1126/science.189.4201.419.

Montagner, J.-P., and L. Guillot (2002), Seismic anisotropy and global geodynamics, *Rev. Mineral. Geochem.*, *51*, 353–385, doi:10.2138/gsrmg.51.1.353.

Nabelek, J., G. Hetenyi, J. Vergne, S. Sapkota, B. Kafle, M. Jiang, H. Su, J. Chen, and B.-S. Huang (2009), Underplating in the Himalaya-Tibet

collision zone revealed by the Hi-CLIMB experiment, *Science*, *325*(5946), 1371–1374, doi:10.1126/science.1167719.

Nabelek, P. I., A. G. Whittington, and A. M. Hofmeister (2010), Strain heating as a mechanism for partial melting and ultrahigh temperature metamorphism in convergent orogens: Implications of temperature-dependent thermal diffusivity and rheology, *J. Geophys. Res.*, *115*, B12417, doi:10.1029/2010JB007727.

Nelson, K. D., et al. (1996), Partially molten middle crust beneath southern Tibet: Synthesis of Project INDEPTH results, *Science*, *274*, 1684–1688, doi:10.1126/science.274.5293.1684.

Ni, J., and M. Barazangi (1984), Seismotectonics of the Himalayan collision zone: Geometry of the underthrusting Indian Plate beneath the Himalaya, *J. Geophys. Res.*, *89*(B2), 1147–1163, doi:10.1029/JB089iB02p01147.

Nolet, G., and F. A. Dahlen (2000), Wave front healing and evolution seismic delay times, *J. Geophys. Res.*, *105*(B8), 19,043–19,054.

Priestley, K., E. Debayle, D. McKenzie, and S. Pilidou (2006), Upper mantle structure of eastern Asia from multimode surface waveform tomography, *J. Geophys. Res.*, *111*, B10304, doi:10.1029/2005JB004082.

Saito, M. (1988), *DISPER80: A Subroutine Package for the Calculation of Seismic Normal-Mode Solutions*, Elsevier, New York.

Silver, P. G. (1996), Seismic anisotropy beneath the continents: Probing the depths of geology, *Annu. Rev. Earth Planet. Sci.*, *24*, 385–432, doi:10.1146/annurev.earth.24.1.385.

Sol, S., et al. (2007), Geodynamics of the southeastern Tibetan Plateau from seismic anisotropy and geodesy, *Geology*, *35*(6), 563–566, doi:10.1130/G23408A.1.

Styron, R., M. Taylor, and K. Okoronkwo (2010), Database of active structures from the Indo-Asian collision, *Eos Trans. AGU*, *91*(20), 181–182, doi:10.1029/2010EO200001.

Tapponnier, P., X. Zhiqin, F. Roger, B. Meyer, N. Arnaud, G. Wittlinger, and Y. Jingsui (2001), Oblique stepwise rise and growth of the Tibet plateau, *Science*, *294*(5547), 1671–1677, doi:10.1126/science.105978.

Tilmann, F., et al. (2003), Seismic Imaging of the downwelling Indian lithosphere beneath central Tibet, *Science*, *300*(5624), 1424–1427, doi:10.1126/science.1082777.

Turner, S., N. Arnaud, J. Liu, C. Hawkesworth, N. Harris, S. Kelly, P. V. Calsteren, and W. Deng (1996), Post-collision, shoshonitic volcanism on the Tibetan Plateau: Implications for convective thinning of the lithosphere and the source of ocean island basalts, *J. Petrol.*, *37*(1), 45–71, doi:10.1093/petrology/37.1.45.

Whittington, A. G., A. M. Hofmeister, and P. I. Nabelek (2009), Temperature-dependent thermal diffusivity of the Earth's crust and implications for magmatism, *Nature*, *458*(7236), 319–321, doi:10.1038/nature07818.

Wittlinger, G., et al. (1996), Seismic tomography of northern Tibet and Kunlun: Evidence for crustal blocks and mantle velocity contrasts, *Earth Planet. Sci. Lett.*, *139*, 263–279, doi:10.1016/0012-821X(95)00235-5.

Yang, Y. J., and D. W. Forsyth (2006), Regional tomographic inversion of the amplitude and phase of Rayleigh waves with 2-D sensitivity kernels, *Geophys. J. Int.*, *166*(3), 1148–1160, doi:10.1111/j.1365-246X.2006.02972.x.

Yang, Y., et al. (2010), Rayleigh wave phase velocity maps of Tibet and the surrounding regions from ambient seismic noise tomography, *Geochem. Geophys. Geosyst.*, *11*, Q08010, doi:10.1029/2010GC003119.

Yin, A., and T. M. Harrison (2000), Geologic evolution of the Himalayan-Tibetan orogen, *Annu. Rev. Earth Planet. Sci.*, *28*, 211–280, doi:10.1146/annurev.earth.28.1.211.

Yue, H., et al. (2012), Lithospheric and upper mantle structure of the northeastern Tibetan Plateau, *J. Geophys. Res.*, *117*, B05307, doi:10.1029/2011JB008545.

Zhao, J., et al. (2010), The boundary between the Indian and Asian tectonic plates below Tibet, *Proc. Natl. Acad. Sci. U. S. A.*, *107*(25), 11,229–11,233, doi:10.1073/pnas.1001921107.

Zhao, W., et al. (2011), Tibetan plate overriding the Asian plate in central and northern Tibet, *Nat. Geosci.*, *4*(12), 870–873, doi:10.1038/ngeo1309.

Zhou, H., and M. Murphy (2005), Tomographic evidence for wholesale underthrusting of India beneath the entire Tibetan plateau, *J. Asian Earth Sci.*, *25*(3), 445–457, doi:10.1016/j.jseaes.2004.04.007.

Zhu, L., and D. V. Helmberger (1998), Moho offset across the northern margin of the Tibetan Plateau, *Science*, *281*, 1170–1172, doi:10.1126/science.281.5380.1170.